PCCP

Accepted Manuscript

Volume 1 | Number 1 | Jan 2013 | Pages 1–100

PCCP

Physical Chemistry Chemical Physics

www.rsc.org/pccp

ROYAL SOCIETY OF CHEMISTRY

ROYAL SOCIETY OF CHEMISTRY

www.rsc.org/pccp

Nitrogen Doped TiO_2/Cu_xO Core/Shell Mesoporous Spherical Hybrids for High-Performance Dye-Sensitized Solar Cells

Enyan Guo, Longwei Yin*

Key Laboratory for Liquid-Solid Structural Evolution and Processing of Materials, Ministry of Education, School of Materials Science and Engineering, Shandong University, Jinan 250061, P. R. China

*To whom correspondence should be addressed. Tel.: + 86 531 88396970. Fax: + 86 531 88396970. E-mail: yinlw@sdu.edu.cn

Abstract We report on high-performance dye-sensitized solar cells (DSSCs) based on nitrogen doped anatase TiO_2/Cu_xO core/shell mesoporous hybrids synthesized through a facile and controlled combined sol-gel and hydrothermal process in the presence of hexadecylamine as the structure-directing agent. The matching of band edges between Cu_xO and TiO_2 to form a semiconductor heterojunction, plays an important role in effective separation of light induced electrons and holes, providing a promising photoanode for DSSCs for its wide absorption spectrum, high electron injection efficiency, and fast electron transference. DSSCs based on the mesoporous TiO_2/Cu_xO core/shell hybrids show a high short-circuit current density of 9.60 mA cm^{-2} and a conversion efficiency of 3.86% under one sun illumination. While DSSCs based on the N-doped mesoporous TiO_2/Cu_xO hybrids exhibit the higher short-circuit current density of 13.24 mA cm^{-2} and a conversion efficiency of 4.57% under one sun illumination. In comparison with un-doped TiO_2/Cu_xO hybrids, the doping of nitrogen into lattice of TiO_2 can extend the light absorption in ultraviolet range to visible light region and effectively decrease the recombination rate of photo-generated electron and holes. The presented N-doped mesoporous TiO_2/Cu_xO hybrids as photoanodes could find potential applications for high performance DSSCs.

Keywords: doping, hybrids, TiO_2, dye-sensitized solar cells, band gap energy

TOC

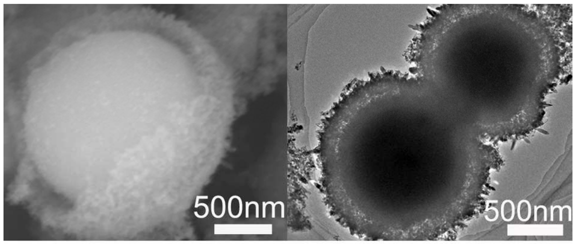

1. Introduction

Dye-sensitized solar cells (DSSCs) are attracting considerable attention because of their diverse advantages such as low cost, environmental benign process and high efficiency.[1,2] Among the various types of oxide semiconductors, titanium Oxide (TiO_2) is widely recognized as the most promising and versatile material for photocatalysis and solar cell applications due to its outstanding physical and chemical properties, including chemical stability, photostability, non-toxicity, inexpensiveness, and appropriate electronic band structure.[3,4] In the past decades, considerable efforts have been concentrated on practical applications for DSSCs based on varieties of nanostructured TiO_2, such as nanocrystals[5,6], nanofibers[7,8], nanotubes[9], inversed opals[10] and mosoporous beads.[11,12] Especially, mesoporous TiO_2 spherical nanostructures have received significant research attention due to their abundant mesopores (2-50 nm), providing a high surface area to maximize the uptake of dye molecules, and enhancing the light-harvesting capability, thereby giving rise to a large current density and high photon-to-current conversion efficiency for the TiO_2 based DSSCs.[13,14]

Unfortunately, one of the deficiencies of TiO_2 is its low efficiency of optical absorption in the visible light region due to its intrinsic wide band gap (Eg = 3.2 eV). Furthermore, the photo-generated electrons and holes can easily recombine, resulting in a large recombination rate for the photo-generated electron-hole pairs. To improve the photoelectron conversion energy efficiency, a variety of strategies have been developed to improve the optical response property and photoelectron energy efficiency, such as coupling with low band gap semiconductors PbS[15], CdTe[16], CdS[17,18], CdSe[19] and PbSe[20], combination with noble metal nanoparticles, doping with non-metal[21,22] and metal ions[4,23,24], and dye sensitization[25]. Especially, narrow band gap semiconductors acting as sensitizers, can effectively facilitate the electron transfer to the conduction band of large band gap TiO_2 in the hybrids of semiconductor/TiO_2 heterojunction, thereby efficiently separating photogenerated charge carriers. As a result, the visible light can be efficiently utilized and the separation rate of photo-generated electron-hole pairs can be substantially increased in the hybrids of narrow band gap semiconductor/TiO_2.

Monoclinic CuO and cubic Cu_2O, as the two main lattice structures of p-type copper oxide, display narrow band gap energy of 1.2～1.85 eV and 2.1 eV, respectively.[26,27] Because of various superiorities of the copper oxides, such as low cost, low toxicity, abundance, and ability to be coupled with a wide band gap semiconductor, copper oxide compounds can be coupled with TiO_2 for application of photocatalysis,[28,29] hydrogen production,[30-32] sensors,[33,34] and solar cells.[35,36] It is great importance to fabricate hybrids of copper oxide nanoparticles sensitized mesoporous anatase TiO_2 with a large surface area for their application in the field of solar cells.

In this work, we reported on nitrogen doped mesoporous TiO_2/Cu_xO core/shell hybrids as photoanodes of DSSCs. In comparison with pure TiO_2, the doping of nitrogen into lattice of TiO_2 can extend the light absorption in ultraviolet range to visible light region and effectively decrease the recombination rate of photo-generated electron and holes, and the formation of mesoporous TiO_2 and Cu_xO can provide a large surface area for dye loading, sufficient light harvesting and efficiently separated photogenerated charge carriers. DSSCs based on the as-synthesized core/shell hybrids of mesoporous TiO_2/Cu_xO core/shell hybrids show a high short-circuit current density of 9.60 mA cm^{-2} and a conversion efficiency of 3.86% under one sun illumination. While DSSCs based on the mesoporous N-doped TiO_2/Cu_xO core/shell hybrids exhibit the higher short-circuit current density of 13.24

mA cm^{-2} and a conversion efficiency of 4.57% under one sun illumination.

2. Experimental

2.1 Preparation of N-doped TiO_2/Cu_xO hybrids

Amorphous precursor TiO_2 beads were synthesized according to literature procedures.[11,37] At room temperature, 2.69 g hexadecylamine was dissolved in 400 mL ethanol under vigorous stirring, followed by the addition of 1.6 mL of 0.1 M KCl solution in the reaction solution. Then, 8.8 mL tetraisopropyl titanate was dropwise added into the solution with keeping constant stirring speed at ambient temperature. The white TiO_2 suspension was kept stillness at the same temperature for 18 h. Finally, the TiO_2 beads were collected on a filter, washed with ethanol three times and dried at room temperature.

TiO_2/Cu_xO hybrids were synthesized through a solvothermal process in the presence of copper acetate monohydrate. A 0.4 g of precursor TiO_2 were dispersed in the solution containing 10mL of ultrapure water and 20 mL of 0.025, 0.05 and 0.1 M concentrations of copper acetate monohydrate in ethanol solution (Corresponding TiO_2/Cu_xO hybrids are denoted as S2, S3 and S4 samples, respectively), respectively. Afterwards, 1.2 mL of 25 wt % ammonia solution was added, respectively. As a comparison, the pure mesoporous anatase TiO_2 beads were also obtained. The 1.6 g precursor TiO_2 beads in a 30 mL ethanol-water mixture (2:1 by volume) containing 0.5 mL of 25 wt % ammonia solutions (denoted as sample S1). This mixed solution was stirred for 10 mins. After that, the mixture was transferred to a Teflon-lined autoclave and heated to 160 °C for 16 h. The resulted precipitates were collected by centrifuged, washed with ethanol and dried in air at room temperature. Finally, the products were calcined at 550 °C for 2 h in air to remove organic components and produce the good crystallinity for characteraction.

Nitrogen doped mesoporous TiO_2/Cu_xO nanoparticles core/shell nanostructures were synthesized according to the above mentioned experimental procedure. The only change is adding 1.8 mL hydrazine hydrate solution after the 8.8 mL tetraisopropyl titanate was dropwise added into mixed solution, the others are unchanged. The N-doped TiO_2/Cu_xO hybrids prepared in 0.025, 0.05 and 0.1 M concentrations of copper acetate monohydrate in ethanol solution are denoted as NS2, NS3 and NS4 samples, respectively.

2.2 Characterization.

X-ray diffraction (XRD) patterns were obtained using a Philips Rigaku D/Max-kA X-ray diffractometer equipped with a Cu Kα source at 40 kV and 30 mA. The surface microstructure and chemical components of the products were analyzed using SU-70 field-emission scanning electron microscopy (FESEM) and attached X-ray energy dispersive spectrometry (EDS). The absorption spectrum and the UV/visible diffuse-reflectance spectra (DRS) were measured by UV-vis spectrophotometry (TU-1900). Nitrogen adsorption-desorption isotherms were determined at 77 K using Gold APP V-Sorb 2800P surface area and porosity 60 analyzer. The surface area measurements were performed according to the Brunauer-Emmett-Teller (BET) method, while the pore size distribution was obtained from the adsorption branch of isotherm using the corrected form of the Kelvin equation by means of the Barrette Joynere Halenda (BJH) method. Dye uptake per unit area (1cm^2) was investigated using UV-Vis spectroscopy (TU-1900) by the dissolution of dye adsorbed the sample films membrane in 0.2 M NaOH water and ethanol (50:50, v/v) solution. The selected-area electron diffraction (SAED) characterization and microstructural analyses were carried out in a Phillips Tecnai 20U-Twin high-resolution transmission electron microscope at an acceleration voltage of 200 kV. Cells were tested using a solar simulator (Newport, Class 3A, 94023A) at one sun (AM1.5G, 100mW cm^{-2}) by a Keithley 2420 source meter equipped with a calibrated Si-reference cell (certificated by NREL). The incident photon to current efficiency (IPCE) measurement was carried out using a QEX 10 system (PV Measurement). A reference Si photodiode calibrated for spectral response was used for the monochromatic power-density calibration. The electrochemical impedance spectra (EIS) were used a Princeton Parstate 2273A in a two-electrode design; the sample films served as a working electrode and the Pt-coated ITO or FTO glass as a counter electrode at an applied bias of the open circuit voltage under one-sun irradiation. The frequency range was 10 mHz to 100 KHz; the magnitude of the alternating potential was 20 mV. The EIS data were analyzed with an appropriate equivalent circuit using simulation software.

2.3 Fabrication of solar cells.

For the working electrode, the fabrication process of the sample paste was described in detail as follows.[38] 0.12 g of ethyl cellulose powders (Aladdin-reagent, China) were dissolved in ethanol to yield a 10 wt% solution. The obtained mixture was added into 0.2 g of the calcined sample and 0.8 g of terpineol (Aladdin-reagent, China) which was diluted with 1.0 mL of ethanol. The mixture was then stirred in a magnet field and sonicated by an ultrasonic horn for three consecutive times. At last, the obtained paste was spin-coated onto a FTO glass substrate with a spin coating apparatus at 2000 rpm for several seconds to obtain a film of the required thickness for repetitive several times. In order to remove the polymer template and organic compounds, the TiO_2 photoelectrode was dried at 125 °C, and gradually heated under flowing air at 325 °C for 5 min, at 375 °C for 5 min, at 450 °C for 15 min and 500 °C for 15 min.

After calcination, the TiO_2 electrodes with an active working area of 0.4*0.4=0.16 cm^2 were immersed into a 0.5 mM dye N-719 ethanol solution in a 1:1 (v/v) mixture of acetonitrile (Aladdin-reagent, China) and *tert*-butanol (Aladdin-reagent, China) at room temperature for 24 h. Subsequently, the dye loaded photoanode and Pt-counter electrode (Dyesol) were assembled into a sandwich type cell and sealed with a spacer of 25μm thickness (Surlyn, DuPont). The internal space of the cell was filled with a liquid electrolyte, which consisted of 0.6 M 1-methy-3- propylimidazolium iodide (PMII), 0.05 M LiI, 0.05 M I_2, and 0.5 M 4-tertbutyl pyridine (TBP) in a (85:15 vol %) mixture of acetonitrile (Aladdin-reagent, China) and valeronitrile (Aladdin-reagent, China).

3. Results and discussion

3.1 Structural characterization

3.1.1 The XRD pattern analysis

The crystalline structure and phase component of the synthesized products were examined by x-ray powder diffraction (XRD). Fig. 1 shows the XRD patterns of TiO_2 and TiO_2/Cu_xO hybrids prepared under different concentrations of copper acetate monohydrate: (a) 0 M, (b) 0.025 M, (c) 0.05 M and (d) 0.1M. Fig. 1a depicts typical wide-angle XRD patterns of the synthesized materials. It is indicated that the synthesized materials after annealing at 550 °C in air are composed of highly crystalline TiO_2 with an anatase structure (PDF: 21-1272) (space group: *I41/amd*) with lattice constants of a = 3.785 Å, c = 9.514 Å. The diffraction peaks at 25.3°, 37.8°, 48°,53.9° and 55° can be well assigned to (101), (004), (200), (105) and (211) planes of crystalline TiO_2, respectively. The XRD patterns in Fig. 1b-1d demonstrate the crystalline structure and phase components of the products obtained after treatment in copper acetate monohydrate ethanol solution. For the XRD patterns of the products, besides the anatase TiO_2, the presence of CuO phase with monoclinic lattice structure and cubic Cu_2O structure can also be determined in the synthesized products. The peaks at 35.5°, 38.7°and 48.7°, correspond well with (002), (111) and (-202) planes of CuO (PDF: 45-0937) (space group: C2/c). The peaks located at 37° and 62.4° can be indexed as (111) and (220) planes of the cubic Cu_2O (PDF: 34-1354) (space group: Pn-3m), respectively. The average size of the CuO and Cu_2O nanoparticles in the as-prepared nanomaterials is estimated from the Debye-Scherrer formula[39] to be about 23.50±1.0 nm, 19.6±1.0 nm, respectively. For the complex of copper oxides composed of Cu_2O and CuO phases, it can be denoted as Cu_xO in the TiO_2/Cu_xO hybrids.

3.1.2 XPS characterization

As is known, pure TiO_2 can only absorb the UV light, which is only a small part of the overall solar energy. Furthermore, in order to extend the light responsibility from ultraviolet range to visible light region to further improve the power conversion efficiency of the DSSCs, [40, 41] anion doping (C, N, F, and S) is proved to be effective to efficiently shift the optical absorption to the visible range of TiO_2.[42-44]

For this reason, we choose hydrazine as the nitrogen sources to dope mesoporous TiO_2 in the TiO_2/Cu_xO core/shell hybrid photoanodes for DSSCs. XPS characterization is conducted to clarify chemical composition component and chemical bonding state of the N-doped TiO_2/Cu_xO core/shell hybrids (NS3). As shown in Fig. 2a, the general survey spectrum for the N-doped TiO_2/Cu_xO nanoparticles contains C, N, Cu, Ti, and O elements. The carbon could have resulted from adventitious hydrocarbons from the XPS instrument itself and can be taken as the standard signal for the correction of other peaks. For the Ti 2p spectrum (Fig. 2b), two main peaks of Ti $2p_{3/2}$ and $2p_{1/2}$ at bonding energies of 458.5 and 464.3 eV, respectively, reveal that Ti ions exist in the form of Ti^{4+} in the lattice of TiO_2.[41,45] Fig. 2c depicts significant N1s peak at 400.9 eV, which can be attributed to the formation of Ti–O–N or Ti–N–O bonding.[46] In the present work, hydrazine was used as the nitrogen source.[47] Fig. 2d shows representative XPS spectra of Cu 2p3 and Cu 2p1. Two fitting peaks for Cu 2p3 at around 933.2 and 932 eV can be assigned to the Cu(II) [48] state and the Cu(I)[49] state, respectively. In addition, the shakeup satellite peaks around 942.7 and 940.5 eV suggest the existence of fully oxidized CuO and incompletely oxidized Cu_2O.[50] the XPS results above on Cu reveal that there coexist two types of phases of CuO or Cu_2O for the copper oxides, which can be denoted as Cu_xO, in good agreement with the XRD results. Fig. 2e displays core-level high-resolution XPS spectra of O1s for the representative the nitrogen doped TiO_2/Cu_xO hybrids. The XPS spectra peak deconvolution of O1s shows a large peak at 529.3 eV, indicating O=O bonding linked to Ti-O or Cu-O structure, and two smaller shoulders located at around 530.6 eV (Ti-O) and 229.2 eV (Cu-O).

3.2 Microstructure characterization

3.2.1 SEM characterization

The micorstructure and morphology of the synthesized mesoporous TiO_2/Cu_xO hybrids were characterized using a SU-70 FESEM. The low- and high-magnification SEM images of S2, S3, and S4 samples were depicted in Fig. 3a-3b, 3c-3d, and 3e-3f, respectively. The sample S2 after calcinations at 550 shows a spherical shape with mesoporous structure with an average diameter of 1.5 μm. According to XRD results, the S2, S3, and S4 samples are composed of anatase TiO_2, Cu_2O and CuO phases. Compared with S2 and S3 samples, a relatively low amount of Cu_2O and CuO phases are deposited on the surface of TiO_2. With the concentration of copper acetate monohydrate increasing to 0.05 M, more and more Cu_2O and CuO phases are deposited on the surface of TiO_2, forming a typical core/shell hybrid structure of mesoporous TiO_2/Cu_xO hybrids (Fig. 3c-3d). In comparison with the sample S1 and S2 samples, the thickness of Cu_xO shell increases to about 50 nm. From high magnification SEM images in Fig. 3b, 3d and 3f, it shows the mesoporous TiO_2/Cu_xO hybrids are composed of mesoporous anatase TiO_2 core and Cu_xO shell. The Cu_xO shell is composed of Cu_2O and CuO nanoparticles. The mesoporous core/shell structured hybrids could provide a large surface area and space to enhance the adsorption of dye and electrolyte, and be helpful to improve the photoelectric conversion efficiency of solar cells.

The elemental energy-dispersive spectroscopy (EDS) mapping characterization was used to investigate the chemical composition component and elemental distribution of the TiO_2/Cu_xO core/shell nanostructures (S4). Fig. 4a shows a low FESEM image of the TiO_2/Cu_xO core/shell nanostructures. The EDS elemental mapping of Ti, O and Cu elements in Fig. 4b-4d shows that Ti, O and Cu elements are homogenously distributed among the whole TiO_2/Cu_xO core/shell nanostructures, suggesting Cu_xO nanoparticles are grown homogeneously onto surfaces of mesoporous anatase TiO_2 matrices. A typical EDS spectrum (Fig. 4e) shows that the products are composed of O, Ti and Cu elements.

3.2.2 TEM characterization

Transmission electron microscopy (TEM) was used to further reveal the microstructures of mesoporous TiO_2/Cu_xO hybrids (S3). The morphology and size distribution and morphology of TiO_2/Cu_xO hybrids are depicted in the low magnification TEM image in Fig. 5a. A magnification TEM image taken from the edge of TiO_2/Cu_xO hybrids in Fig. 5a is illustrated in Fig. 5b. It is clearly shown that the mesoporous hybrid is composed of TiO_2 and Cu_xO nanocrystals. A HRTEM lattice image of the single TiO_2 nanoparticle is given in Fig. 5c. The marked d-spacing of 0.13 nm and 0.10 nm correspond well to that of (22-2) and (-231) planes of anatase TiO_2. Fig. 5d shows a monoclinic CuO nanocrystal with clear crystalline lattice fringes. The fringe spacing of 0.17 nm corresponds to the (311) planes, while the fringe spacing of 0.13 nm corresponds to the (020) planes. While in a HRTEM lattice image of the TiO_2/Cu_xO hybrid of Fig. 5e, the marked d-spacing of 0.35 nm and 0.23 nm is in agreement with that of (101) plane of TiO_2 and (111) plane of CuO. The diffraction rings in Fig. 5f correspond well with (101), (200) and (211) planes of anatase TiO_2 and (111) plane of monoclinic CuO, respectively.

TEM examination was carried out on the sample S4 to investigate the effects of concentration of copper acetate monohydrate on the microstructures of the TiO_2/Cu_xO hybrid samples (Fig. 6). It can be seen that the sample S4 displays typical core/shell structure with mesoporous anatase TiO_2 acting as the core section and the Cu_xO as the shell section (Fig. 6a), and this is consistent with the FESEM images in Fig. 3f. Fig. 6b depicts a high magnification TEM image taken from the shell's edge of TiO_2/Cu_xO core/shell nanostructures, showing Cu_xO nanoparticles with the size ranging from 20 to 30 nm to form a Cu_xO shell with a thickness of 150 nm. Fig. 6c demonstrates a HRTEM lattice image of an anatase TiO_2 nanocrystal and a monoclinic CuO nanoparticle. The marked d-spacing of 0.35 nm and 0.35 nm correspond well to (-101) and (01-1) planes of anatase TiO_2. The marked d-spacing of 0.20 nm and 0.16 nm correspond well to (1-1-2) and (02-1) planes of monoclinic CuO. Fig.

6d displays a typical SAED pattern of the samples. The diffraction rings are in agreement with (101), (200) and (211) planes of anatase TiO_2 and (111) planes of monoclinic CuO, respectively.

3.2.3 Optical properties

The optical properties of mesoporous TiO_2 and TiO_2/Cu_xO core/shell hybrids were investigated by UV−visible diffuse reflectance spectra. Fig. 7a shows the diffuse reflectance spectra (DRS) of (a) pure TiO_2 (S1) and TiO_2/Cu_xO samples (S2-S4), respectively. The pure TiO_2 sample shows a sharp absorption edge around 380 nm, which is typical for anatase TiO_2. It is interesting to observe that the core/shell TiO_2/Cu_xO hybrids show a continuous absorption in the visible range, which can be primarily ascribed by the coupling of the narrow band gap Cu_xO nanoparticles with TiO_2, effectively extending the optical response to visible region from ultraviolet region. Furthermore, the intensity of UV−visible diffuse reflectance spectra becomes stronger after the Cu_xO shell is introduced to form the core/shell TiO_2/Cu_xO hybrids. The band gap energy of the mesoporous TiO_2 and TiO_2/Cu_xO hybrids can be roughly determined according to the plots in Fig. 7b, which are obtained via the transformation based on the Kubelka-Munk function ($F(R\infty)=(1-R)^2/(2R)$, where R is the reflection coefficient).[53] The estimated band-gap energy of the mesoporous TiO_2/Cu_xO hybrids with different Cu_xO loading contents (S1, S2, S3, S4 samples), corresponds approximately to the light responsibility with an energy band gap of 3.20, 2.98, 2.73 and 2.94 eV, respectively. Therefore, it can be concluded that the sample S3 has the best light absorbing and the transition of light responsibility from UV to visible light of the TiO_2/Cu_xO samples can be realized by controlling the contents of Cu_xO nanoparticles. It is obvious that the optical properties of the TiO_2/Cu_xO samples can be tuned by adjusting the concentration of copper acetate monohydrate.

In order to further improve the photoelectron conversion efficiency (η) of solar cells, we synthesize mesoporous N-doped TiO_2/Cu_xO core/shell hybrids. Fig. 7c shows the UV−visible diffuse reflectance optical properties of the N-doped TiO_2/Cu_xO hybrids spectra (DRS) of (a) NS1, NS2, NS3, NS4 samples. It is observed that the N-doped TiO_2/Cu_xO hybrids show continuous absorption in the visible range. The absorption edge for pure TiO_2 is observed at 385 nm (～3.2 eV), while the absorption edge of the N-doped TiO_2 sample (NS1) is at around 415 nm (～3.0 eV). Compared to un-doped TiO_2/Cu_xO core/shell hybrids (S2, S3, and S4 samples), the N-doped TiO_2/Cu_xO core/shell hybrids (NS2, NS3 and NS4 samples), and drastic red-shift takes place towards the visible spectral range. It could be ascribed to the combined effect of the doping-induced mid-gap electronic states and the lattice disorder effects due to the nitrogen doping. In the N-TiO_2 system the visible-light response arises due to occupied localized N2p states above the valence band. The doping also creates localized states below the conduction band edge.[51, 52]

The band gap energy of the samples can be roughly confirmed according to the plots in Fig. 7d, which is obtained via the transformation based on the Kubelka-Munk function ($F(R\infty) = (1-R)^2/(2R)$, where R is the reflection coefficient).[53] The N-doped TiO_2 sample exhibits a smooth absorption edge around 415 nm, corresponding to band gap energy of 3.0 eV. The estimated band gap value of the N-doped TiO_2/Cu_xO hybrids corresponds approximately to 3.00, 2.92, 2.81 and 2.70 eV for NS1, NS2, NS3, NS4 samples, respectively.

3.2.4 Nitrogen adsorption-desorption curves

Table 1 Structural property of the TiO_2, TiO_2/Cu_xO and N-doped TiO_2/Cu_xO samples

Samples	BET surface area/$m^2\ g^{-1}$	Pore diameter/nm	Total pore volume/$cm^3\ g^{-1}$

S1	73.08	17.80	0.395
S2	51.92	25.12	0.587
S3	62.64	21.99	0.478
S4	75.28	16.13	0.469
NS1	68.56	27.29	0.612
NS3	54.67	39.13	0.591

The nitrogen adsorption-desorption isotherms and the corresponding pore size distribution curves determined at 77K by the BJH method of the TiO_2 (S1), TiO_2/Cu_xO of S2, S3, S4 materials prepared under different concentrations of copper acetate monohydrate: (a) 0 M, (b) 0.025 M, (c) 0.05 M and (d) 0.1 M, the N-doped TiO_2/Cu_xO of NS1, NS3 are all shown in Fig. 8. As shown in the isotherms, all the materials exhibit type IV characteristic (based on IUPAC classification) and the typical H1 hysteresis loop. The capillary condensation occurs at a relative pressure of $(P/P_0) \approx 0.60\text{-}0.95$, indicating a uniform mesopore diameter distribution. The textural parameters such as specific surface area, pore diameter and pore volume of the TiO_2 and TiO_2/Cu_xO samples are summarized in Table 1. The TiO_2 sample displays a specific surface area of about 73.08 $m^2\ g^{-1}$ and pore volume of 17.80 $cm^3\ g^{-1}$, respectively. It is shown that the coupling of mesoporous TiO_2 and Cu_xO nanoparticles results in an increase of surface area and decrease of pore volume of the core/shell hybrids. This can be confirmed by the increased condensation step of the TiO_2/Cu_xO hybrid samples in Fig. 8a. With the concentration of copper acetate monohydrate, the specific surface area of the TiO_2/Cu_xO hybrids increases from 51.92 for S2 sample, 62.64 for S3 sample, and finally to 75.28 m^2g^{-1} for S4 sample, respectively. While the pore size of the TiO_2/Cu_xO hybrids deceases from 25.12 nm for S2 sample, to 16.33 nm for S4 samples, respectively. For the N-doped TiO_2/Cu_xO of NS1, NS3, as shown in table 1, the specific surface area is larger than that of S1, S3, S4 samples, while the pore diameter and pore volume of NS1 and NS3 samples are larger than that of S1-S4 samples, respectively.

3.3 The performance of solar cells

3.3.1 Eectrochemical impedance spectroscopy (EIS) analysis

In order to better understand the kinetics of electrochemical and photoelectrochemical processes occurring in DSSCs, the analysis of electrochemical impedance spectroscopy (EIS) of DSSCs was performed under illumination and open-circuit voltage. Fig. 9 demonstrates that the Nyquist plots displaying two semicircles with a contact series resistance (Rs) on the FTO substrate. The smaller and larger semicircles in the Nyquist plots are attributed to the charge transfer at the electrode/electrolyte interface and the working electrode/dye/electrolyte interface, respectively. The sheet resistance (Rs) of the substrate, charge transfer resistance of the counter electrode (R_1) and recombination resistance (R_2) were analyzed by ZSimpWin software using an equivalent circuit containing a constant phase element (CPE) and resistances (R) (Fig. 9, inset). The cells based on the P25, S1, S3, NS1(N denotes represents nitrogen-doped) and NS3 samples posses almost the same value of 4.0 Ω for Rs, and R1 of 28.7, 30.1, 29.9, 24.2 and 29.1Ω, respectively, due to the use of the same counter electrode (Pt/FTO glass) and electrolyte. The recombination resistance (R_2) of the samples is 67.7, 67.9, 56.8, 56.7 and 36.9 Ω, respectively.

3.3.2 The performance of solar cells

Table 2 Performances of solar cells based on the P25 and the synthesised samples under simulated AM 1.5 illuminations.

samples	Voc (V)	Jsc (mA cm^{-2})	Fill Factor (%)	η^a (%)	Dye adsorption (nmol cm^{-2})
P25	0.69	6.94	55.82	2.67	65.51
S1	0.67	8.01	61.49	3.30	78.65
S2	0.63	8.62	64.52	3.54	60.92
S3	0.62	9.60	64.85	3.86	68.50
S4	0.68	9.43	59.55	3.82	86.27
NS1	0.64	11.70	56.55	4.23	70.45
NS2	0.65	12.62	51.71	4.24	58.67
NS3	0.66	13.24	52.26	4.57	59.40
NS4	0.66	13.02	52.38	4.50	73.74

a) η (%) = $J_{sc}V_{oc}$ FF/ P_{in}, where P_{in} = 100 mW cm^{-2} (AM 1.5). Each η is an average value obtained from 5 samples.

The dye adsorbing capacity and the photovoltaic performance of DSSCs based on (b) S1, (c) S2 and (d) S3 film electrodes were examined comparatively with that of the (a) P25 photoelectrode, as listed in Table 2. The photocurrent density-voltage (J-V) characteristics of these DSSCs are shown in Fig. 10. In comparison with P25 cell, the S1 cell exhibits a similar open-circuit voltage (Voc) and FF, yet larger short-circuit current density (Jsc) and higher conversion efficiency (η). This is mainly attributed to the larger surface area of the S1, helpful to absorb more dye molecules on the surface.

For the S2, S3 and S4 cells, the photoelectron conversion efficiency (η) can maintain 3.54%, 3.86%, 3.82%, respectively. It is suggested that for the Cu_xO sensitized TiO_2 samples, the short-circuit current density (Jsc) and conversion efficiency (η) of the S2-S4 cells are higher than the S1 cell, which is attributed to the large amount of dye adsorption, sufficient light harvesting in the visible region, and fast charge transport. Firstly, the capacity of absorbed dye exerts a profound influence on the photocurrent density. In this regard, the amount of adsorbed N719 dyes can be estimated by measuring the eluted dye molecules using UV-vis absorption spectroscopy.[40] The TiO_2/Cu_xO core/shell hybrids display typical mesoporous characteristics with a large specific surface area and narrow pore diameter (Table1), which can adsorb a larger amount of dye molecules.

Secondly, after coupling Cu_xO nanoparticles with the mesoporous anatase TiO_2, the TiO_2/Cu_xO core/shell nanohybrids display a distinct red shift to the visible light region with longer wavelength for absorption edge (Fig. 7a). The S3 sample shows the mostly enhanced ability to absorb visible-light, and a stronger scattering is revealed from diffuse reflectance measurement for S3 sample in comparison with other samples (Fig. 7a), suggesting an improved light harvesting efficiency, and thus higher short circuit current Jsc.[54-57]

Finally, the electrochemical impedance spectroscopy (EIS) analysis of DSSCs fabricated based on P25, TiO_2/Cu_xO nanohybrids of S1, S2, S3, S4 samples was performed to elucidate the characteristics of charge transfer ability. As shown in Fig. 9, it is clearly shown that the sheet resistance (Rs) of substrate for the three samples is almost same (4Ω). The R1 of the samples are 28.7, 30.1, 29.9Ω, however, the recombination resistance (R_2) of the samples are 67.7, 67.9, 56.8Ω, respectively. The EIS analysis suggested that as compared to pure TiO_2 (P25), moseporous TiO_2 (S1 sample), the formation of mesoporous TiO_2/Cu_xO core/shell hybrids facilitates the charge and electron transfer[58], which indicates that electrons are easier to move at the surface and contribute to the charge transport at the photoanode.

The incident photon to current efficiency (IPCE) measurement was carried out using a QEX 10 system (PV Measurement). The IPCE spectra were added in Figure 11 in the revised manuscript, and corresponding analysis and discussion is added as following: "The corresponding incident monochromatic photon-to-electron conversion efficiency (IPCE) spectra of DSSCs based on of P25, S1, S3, NS1, NS3 samples, are plotted in Fig. 11. The DSSCs samples show a similar feature along the entire wavelength in a range of 400-750 nm. The IPCE results were consistent with the photovoltaic performance of the DSSCs samples. Especially, the DSSCs samples based on NS1 and NS3 exhibit a higher IPCE along the scanned wavelength in comparison with DSSCs based on S1, S2, P25. The variation trend of IPCE spectra of DSSC based on N-doped photoanode clearly reveal the effect of the N doping on the photovoltaic performance of DSSCs based on the N-doped sample. It is shown that the photoelectric response of the N doped photoanodes is enhanced and the electron density increases. Also, it is demonstrated that the IPCE of DSSCs based on NS3 sample display the highest IPCE over the whole wavelength among all the samples. The improvement of IPCE can be attributed to decreased recombination rate of photogenerated electrons and holes, due to N-doping and heterostructure formation between TiO_2 and copper oxide.".

Comparison of the J–V characteristics of DSSCs based on (e) NS1, (f) NS2, (g) NS3 and (i) NS4 film electrodes are shown in Fig. 10. Open-circuit photovoltage (Voc), corresponding short-circuit photocurrent density (Jsc), fill factor of the cell (FF), power conversion efficiency (η), and dye adsorption are listed in Table 2. Compared to the conversion efficiency of undoped TiO_2/Cu_xO core/shell hybrids, the N-doped TiO_2/Cu_xO hybrids display greatly improved solar cell performance, with conversion efficiency of 4.23, 4.24, 4.57, 4.5 for NS1, NS2, NS3, NS4 samples. In comparison to the mesoporous TiO_2/Cu_xO hybrids, the improved performance of the solar cells based on the N-doped TiO_2/Cu_xO core/shell hybrids can be attributed to the higher light scattering ability, which enhances the utilization of solar light,[59,60] the band gap of the nitrogen doped TiO_2/Cu_xO is more narrow than the pure TiO_2/Cu_xO, the faster electron transport of the interfaces, which is confirmed by the electrochemical impedance spectroscopy (EIS) (Fig. 9), the recombination resistance (R_2) of the S1, NS1, S3 and NS3 is 67.9, 56.7, 56.8 and 36.9 Ω, respectively. It is well shown that the NS3 has the smallest recombination resistance (R_2); namely, NS3 has the highest open-circuit. The performance of the solar cell based on the N-doped TiO_2/Cu_xO hybrids materials can be comparable to related materials prepared via the other methods. For example, Sun[35] reported the optimal short-circuit photocurrent and EQE values of the Cu_xO modified TiO_2 nanorod arrays can increase by more than five and nine times compared to the pristine TiO_2, respectively. The performance of DSSCs based on 0.3wt% Cu_2O/N-doped TiO_2 hybrid is better than the undoped TiO_2-based DSSCs by Koo.[61]

The highest power conversion efficiency of DSSCs based on the N-doped TiO_2/Cu_xO materials (NS3) photoanode is 4.57%, which is higher than 3.86% for S3, 3.30% for S1, and 2.67% for P25, respectively. A great enhancement in power conversion efficiency of NS3 photoanode can be obtained compared to that of S3. Hence, the higher short-circuit current density and conversion efficiency of the solar cells based on N-doped TiO_2/Cu_xO core/shell hybrids could be attributed to the larger surface area for adsorbing more dyes, and higher light scattering ability for enhancing the utilization of solar light, which were confirmed by the aforementioned dye adsorption, IPCE and UV-vis diffuse reflectance measurements. As excited by incident photons, the photoelectrons in Cu_xO migrate to the conduction band of TiO_2, and the holes gather in the valence band of the Cu_xO. During this process, the lifetime of the charge carriers can increase, thus, the recombination of electron-hole pairs is further inhibited, finally resulting in an improved photoelectrical performance.[38]

4 Conclusions

We for the first time fabricated N-doped mesoporous TiO_2/Cu_xO core/shell hybrids. The matching of band edges between Cu_xO and TiO_2 to form a semiconductor heterojunction, plays an important role in the effective separation of light induced electrons and holes, providing a promising photoanode for its wide absorption spectrum, high electron injection efficiency, and fast electron transference. DSSCs based on the mesoporous TiO_2/Cu_xO core/shell hybrids show a high short-circuit current density of 9.60 mA cm^{-2} and a conversion efficiency of 3.86% under one sun illumination. Further more, DSSCs based on the N-doped mesoporous TiO_2/Cu_xO hybrids exhibit the higher short-circuit current density of 13.24 mA cm^{-2} and a conversion efficiency of 4.57% under one sun illumination. The performance improvement of the solar cells based Cu_xO nanoparticels/mesoporous anatase TiO_2 beads nanostructures can be attributed to the larger surface area adsorbing a large amount of dye molecules, the improved light harvesting efficiency by a distinct red shift moving to visible light region and the electron transport facilitated by the heterojunction of TiO_2/Cu_xO, and the decrease of recombination rate of photogenerated electron-holes due to the N doping into lattice of TiO_2 and the semiconductor heterostructure between TiO_2 and Cu_xO.

Acknowledgment

We acknowledge support from the National Natural Science Funds for Distinguished Young Scholars (No: 51025211), National Nature Science Foundation of China (No: 51272137), the Tai Shan Scholar Foundation of Shandong Province.

References

1. O'Regan, B.; Gratzel, M., A low-cost, high-efficiency solar cell based on dye-sensitized colloidal TiO_2 films. *Nature* **1991,** *353* (6346), 737-740.

2. Wu, X.; Chen, Z.; Lu, G. Q. M.; Wang, L., Nanosized Anatase TiO_2 Single Crystals with Tunable Exposed (001) Facets for Enhanced Energy Conversion Efficiency of Dye-Sensitized Solar Cells. *Adv Funct Mater* **2011,** *21* (21), 4167-4172;

3. Chen, X.; Mao, S. S., Titanium dioxide nanomaterials: Synthesis, properties, modifications, and applications. *Chem Rev* **2007,** *107* (7), 2891-2959.

4. Li, Y.; Wang, H.; Feng, Q.; Zhou, G.; Wang, Z.-S., Gold nanoparticles inlaid TiO_2 photoanodes: a superior candidate for high-efficiency dye-sensitized solar cells. *Energ Environ Sci* **2013,** *6* (7), 2156-2165.

5. Wu, X.; Chen, Z. G.; Lu, G. Q.; Wang, L. Z., Nanosized Anatase TiO_2 Single Crystals with Tunable Exposed (001) Facets for Enhanced Energy Conversion Efficiency of Dye-Sensitized Solar Cells. *Adv Funct Mater* **2011,** *21* (21), 4167-4172.

6. Shiu, J. W.; Lan, C. M.; Chang, Y. C.; Wu, H. P.; Huang, W. K.; Diau, E. W. G., Size-Controlled Anatase Titania Single Crystals with Octahedron-like Morphology for Dye-Sensitized Solar Cells. *Acs Nano* **2012,** *6* (12), 10862-10873.

7. Hwang, S. H.; Roh, J.; Jang, J., Nanosilver-decorated TiO_2 nanofibers coated with a SiO_2 layer for enhanced light scattering and localized surface plasmons in dye-sensitized solar cells. *Chemistry* **2013,** *19* (39), 13120-6.

8. Zhang, X.; Thavasi, V.; Mhaisalkar, S. G.; Ramakrishna, S., Novel hollow mesoporous 1D TiO_2 nanofibers as photovoltaic and photocatalytic materials. *Nanoscale* **2012,** *4* (5), 1707-16.

9. Mor, G. K.; Shankar, K.; Paulose, M.; Varghese, O. K.; Grimes, C. A., Use of Highly-Ordered TiO_2 Nanotube Arrays in Dye-Sensitized Solar Cells. *Nano Lett* **2005,** *6* (2), 215-218.

10. Somani, P. R.; Dionigi, C.; Murgia, M.; Palles, D.; Nozar, P.; Ruani, G., Solid-state dye PV cells using inverse opal TiO_2 films. *Sol Energ Mat Sol C* **2005,** *87* (1–4), 513-519.

11. Chen, D. H.; Huang, F. Z.; Cheng, Y. B.; Caruso, R. A., Mesoporous Anatase TiO_2 Beads with High Surface Areas and Controllable Pore Sizes: A Superior Candidate for High-Performance Dye-Sensitized Solar Cells. *Adv Mater* **2009,** *21* (21), 2206-2210.

12. Stefik, M.; Heiligtag, F. J.; Niederberger, M.; Grätzel, M., Improved Nonaqueous Synthesis of TiO2 for Dye-Sensitized Solar Cells. *Acs Nano* **2013,** *7* (10), 8981-8989.

13. Barbé, C. J.; Arendse, F.; Comte, P.; Jirousek, M.; Lenzmann, F.; Shklover, V.; Grätzel, M., Nanocrystalline Titanium Oxide Electrodes for Photovoltaic Applications. *J Am Ceram Soc* **1997,** *80* (12), 3157-3171.

14. Chou, T. P.; Zhang, Q.; Russo, B.; Fryxell, G. E.; Cao, G., Titania Particle Size Effect on the Overall Performance of Dye-Sensitized Solar Cells. *J. Phys. Chem. C* **2007,** *111* (17), 6296-6302.

15. Cahen, D.; Hodes, G.; Grätzel, M.; Guillemoles, J. F.; Riess, I., Nature of Photovoltaic Action in Dye-Sensitized Solar Cells. *J. Phys. Chem. B* **2000,** *104* (9), 2053-2059.

16. Yang, Y.; Rodriguez-Cordoba, W.; Xiang, X.; Lian, T. Q., Strong Electronic Coupling and Ultrafast Electron Transfer between PbS Quantum Dots and TiO_2 Nanocrystalline Films. *Nano Lett* **2012,** *12* (1), 303-309.

17. Lin, X. Y.; Wang, C. L.; Xu, S. H.; Cui, Y. P., Manipulation of inter-particle interactions between TiO_2 and CdTe: an effective method to enhance the performance of quantum dot sensitized solar cells. *J Phys D Appl Phys* **2014,** *47* (1).

18. Lin, S. C.; Lee, Y. L.; Chang, C. H.; Shen, Y. J.; Yang, Y. M., Quantum-dot-sensitized solar cells: Assembly of

CdS-quantum-dots coupling techniques of self-assembled monolayer and chemical bath deposition. *Appl Phys Lett* **2007,** *90* (14).

19. Chang, C.-H.; Lee, Y.-L., Chemical bath deposition of CdS quantum dots onto mesoscopic TiO_2 films for application in quantum-dot-sensitized solar cells. *Appl Phys Lett* **2007,** *91* (5), 053503.

20. Shen, Y. J.; Lee, Y. L., Assembly of CdS quantum dots onto mesoscopic TiO_2 films for quantum dot-sensitized solar cell applications. *Nanotechnology* **2008,** *19* (4).

21. Shen, Q.; Arae, D.; Toyoda, T., Photosensitization of nanostructured TiO_2 with CdSe quantum dots: effects of microstructure and electron transport in TiO_2 substrates. *Journal of Photochemistry and Photobiology A: Chemistry* **2004,** *164* (1-3), 75-80.

22. Tisdale, W. A.; Williams, K. J.; Timp, B. A.; Norris, D. J.; Aydil, E. S.; Zhu, X. Y., Hot-electron transfer from semiconductor nanocrystals. *Science* **2010,** *328* (5985), 1543-7.

23. Naphade, R. A.; Tathavadekar, M.; Jog, J. P.; Agarkar, S.; Ogale, S., Plasmonic light harvesting of dye sensitized solar cells by Au-nanoparticle loaded TiO_2 nanofibers. *J Mater Chem A* **2014,** *2* (4), 975-984.

24. Lei, B. X.; Luo, Q. P.; Yu, X. Y.; Wu, W. Q.; Su, C. Y.; Kuang, D. B., Hierarchical TiO_2 flowers built from TiO_2 nanotubes for efficient Pt-free based flexible dye-sensitized solar cells. *Phys Chem Chem Phys* **2012,** *14* (38), 13175-13179.

25. Zhang, X.; Liu, F.; Huang, Q.-L.; Zhou, G.; Wang, Z.-S., Dye-Sensitized W-Doped TiO_2 Solar Cells with a Tunable Conduction Band and Suppressed Charge Recombination. *J. Phys. Chem. C* **2011,** *115* (25), 12665-12671.

26. Sun, Z.; Zhang, R.-K.; Xie, H.-H.; Wang, H.; Liang, M.; Xue, S., Nonideal Charge Recombination and Conduction Band Edge Shifts in Dye-Sensitized Solar Cells Based on Adsorbent Doped Poly(ethylene oxide) Electrolytes. *J. Phys. Chem. C* **2013,** *117* (9), 4364-4373.

27. Zhao, W.; Sun, Y. L.; Castellano, F. N., Visible-light induced water detoxification catalyzed by Pt-II dye sensitized titania. *J Am Chem Soc* **2008,** *130* (38), 12566-12567.

28. Vaseem, M.; Umar, A.; Kim, S. H.; Hahn, Y. B., Low-temperature synthesis of flower-shaped CuO nanostructures by solution process: Formation mechanism and structural properties. *J. Phys. Chem. C* **2008,** *112* (15), 5729-5735.

29. Yu, H. G.; Yu, J. G.; Liu, S. W.; Mann, S., Template-free hydrothermal synthesis of CuO/Cu_2O composite hollow microspheres. *Chem Mater* **2007,** *19* (17), 4327-4334.

30. Xu, B.; Dong, L.; Chen, Y., Influence of CuO loading on dispersion and reduction behavior of CuO/TiO_2 (anatase) system. *J Chem Soc Faraday T* **1998,** *94* (13), 1905-1909.

31. Zhang, J.; Zhu, H.; Zheng, S.; Pan, F.; Wang, T., TiO_2 film/Cu_2O microgrid heterojunction with photocatalytic activity under solar light irradiation. *ACS Appl Mater Interfaces* **2009,** *1* (10), 2111-4.

32. Wang, M. Y.; Sun, L.; Lin, Z. Q.; Cai, J. H.; Xie, K. P.; Lin, C. J., p-n Heterojunction photoelectrodes composed of Cu_2O-loaded TiO_2 nanotube arrays with enhanced photoelectrochemical and photoelectrocatalytic activities. *Energ Environ Sci* **2013,** *6* (4), 1211-1220.

33. Mor, G. K.; Varghese, O. K.; Wilke, R. H. T.; Sharma, S.; Shankar, K.; Latempa, T. J.; Choi, K. S.; Grimes, C. A., p-type Cu-Ti-O nanotube arrays and their use in self-biased heterojunction photoelectrochemical diodes for hydrogen generation. *Nano Lett* **2008,** *8* (7), 1906-1911.

34. Lalitha, K.; Sadanandam, G.; Kumari, V. D.; Subrahmanyam, M.; Sreedhar, B.; Hebalkar, N. Y., Highly Stabilized and Finely Dispersed Cu_2O/TiO_2: A Promising Visible Sensitive Photocatalyst for Continuous Production of Hydrogen from Glycerol:Water Mixtures. *J. Phys. Chem. C* **2010,** *114* (50), 22181-22189.

35. Yin, Z. Y.; Wang, Z.; Du, Y. P.; Qi, X. Y.; Huang, Y. Z.; Xue, C.; Zhang, H., Full Solution-Processed Synthesis of All Metal Oxide-Based Tree-like Heterostructures on Fluorine-Doped Tin Oxide for Water Splitting. *Adv Mater* **2012,** *24* (39), 5374-5378.

36. Deng, S.; Tjoa, V.; Fan, H. M.; Tan, H. R.; Sayle, D. C.; Olivo, M.; Mhaisalkar, S.; Wei, J.; Sow, C. H., Reduced Graphene Oxide Conjugated Cu_2O Nanowire Mesocrystals for High-Performance NO_2 Gas Sensor. *J Am Chem Soc* **2012,** *134* (10), 4905-4917.

37. Barreca, D.; Carraro, G.; Comini, E.; Gasparotto, A.; Maccato, C.; Sada, C.; Sberveglieri, G.; Tondello, E., Novel Synthesis and Gas Sensing Performances of CuO-TiO_2 Nanocomposites Functionalized with Au Nanoparticles. *J. Phys. Chem. C* **2011,** *115* (21), 10510-10517.

38. Sun, Q.; Li, Y.; Sun, X. M.; Dong, L. F., Improved Photoelectrical Performance of Single-Crystal TiO_2 Nanorod Arrays by Surface Sensitization with Copper Quantum Dots. *Acs Sustain Chem Eng* **2013,** *1* (7), 798-804.

39. Ruhle, S.; Barad, H. N.; Bouhadana, Y.; Keller, D. A.; Ginsburg, A.; Shimanovich, K.; Majhi, K.; Lovrincic, R.; Anderson, A. Y.; Zaban, A., Combinatorial solar cell libraries for the investigation of different metal back contacts for TiO_2-Cu_2O hetero-junction solar cells. *Phys Chem Chem Phys* **2014,** *16* (15), 7066-73.

40. Ye, M.; Xin, X.; Lin, C.; Lin, Z., High Efficiency Dye-Sensitized Solar Cells Based on Hierarchically Structured Nanotubes. *Nano Lett* **2011,** *11* (8), 3214-3220.

41. Tian, H.; Hu, L.; Zhang, C.; Liu, W.; Huang, Y.; Mo, L.; Guo, L.; Sheng, J.; Dai, S., Retarded Charge Recombination in Dye-Sensitized Nitrogen-Doped TiO_2 Solar Cells. *J. Phys. Chem. C* **2010,** *114* (3), 1627-1632.

42. Yu, J.; Dai, G.; Xiang, Q.; Jaroniec, M., Fabrication and enhanced visible-light photocatalytic activity of carbon self-doped TiO_2 sheets with exposed {001} facets. *J Mater Chem* **2011,** *21* (4), 1049-1057.

43. Xiang, Q.; Yu, J.; Jaroniec, M., Nitrogen and sulfur co-doped TiO_2 nanosheets with exposed {001} facets: synthesis, characterization and visible-light photocatalytic activity. *Phys Chem Chem Phys* **2011,** *13* (11), 4853-4861.

44. Ho, W.; Yu, J. C.; Lee, S., Synthesis of hierarchical nanoporous F-doped TiO_2 spheres with visible light photocatalytic activity. *Chem Commun* **2006,** (10), 1115-1117.

45. Cao, J. L.; Shao, G .S.; Ma, T. Y.; Wang, Y.; Ren, T. Z.; Wu, S. H.; Yuan, Z. Y., Hierarchical meso–macroporous titania-supported CuO nanocatalysts: preparation, characterization and catalytic CO oxidation. *J Mater Sci* **2009,** *44* (24), 6717-6726.

46. Jagadale, T. C.; Takale, S. P.; Sonawane, R. S.; Joshi, H. M.; Patil, S. I.; Kale, B. B.; Ogale, S. B., N-Doped TiO_2 Nanoparticle Based Visible Light Photocatalyst by Modified Peroxide Sol−Gel Method. *J. Phys. Chem. C* **2008,** *112* (37), 14595-14602.

47. Chaudhari, N. S.; Warule, S. S.; Dhanmane, S. A.; Kulkarni, M. V.; Valant, M.; Kale, B. B., Nanostructured N-doped TiO_2 marigold flowers for an efficient solar hydrogen production from H_2S. *Nanoscale* **2013,** *5* (19), 9383-9390.

48. Espinós, J. P.; Morales, J.; Barranco, A.; Caballero, A.; Holgado, J. P.; González-Elipe, A. R., Interface Effects for Cu, CuO, and Cu_2O Deposited on SiO_2 and ZrO_2. XPS Determination of the Valence State of Copper in Cu/SiO_2 and Cu/ZrO_2 Catalysts. *J. Phys. Chem. B* **2002,** *106* (27), 6921-6929.

49. Borgohain, K.; Murase, N.; Mahamuni, S., Synthesis and properties of Cu_2O quantum particles. *J Appl Phys* **2002,** *92* (3), 1292-1297.

50. Chusuei, C. C.; Brookshier, M. A.; Goodman, D. W., Correlation of Relative X-ray Photoelectron Spectroscopy Shake-up Intensity with CuO Particle Size. *Langmuir* **1999,** *15* (8), 2806-2808.

51. Serpone, N., Is the Band Gap of Pristine TiO_2 Narrowed by Anion- and Cation-Doping of Titanium Dioxide in Second-Generation Photocatalysts? *J. Phys. Chem.B* **2006,** *110* (48), 24287-24293.

52. Di Valentin, C.; Pacchioni, G.; Selloni, A., Origin of the different photoactivity of N-doped anatase and rutile TiO_2.*Phys Rev B* **2004,** *70* (8), 085116.

53. Uddin, M. T.; Nicolas, Y.; Olivier, C.; Toupance, T.; Servant, L.; Muller, M. M.; Kleebe, H. J.; Ziegler, J.; Jaegermann, W., Nanostructured SnO_2-ZnO heterojunction photocatalysts showing enhanced photocatalytic activity for the degradation of organic dyes. *Inorg Chem* **2012,** *51* (14), 7764-73.

54. Shao, F.; Sun, J.; Gao, L.; Yang, S.; Luo, J., Template-free synthesis of hierarchical TiO_2 structures and their application in dye-sensitized solar cells. *ACS Appl Mater Interfaces* **2011,** *3* (6), 2148-53.

55. Chen, X.; Burda, C., Photoelectron Spectroscopic Investigation of Nitrogen-Doped Titania Nanoparticles. *J. Phys. Chem.B* **2004,** *108* (40), 15446-15449.

56. Guo, W.; Shen, Y.; Boschloo, G.; Hagfeldt, A.; Ma, T., Influence of nitrogen dopants on N-doped TiO2 electrodes and their applications in dye-sensitized solar cells. *Electrochim Acta* **2011,** *56* (12), 4611-4617.

57. Diker, H.; Varlikli, C.; Stathatos, E., N-doped titania powders prepared by different nitrogen sources and their application in quasi-solid state dye-sensitized solar cells. *Int. J. Energy Res.***2014,** *38* (7), 908-917.

58. Kho, Y. K.; Iwase, A.; Teoh, W. Y.; Mädler, L.; Kudo, A.; Amal, R., Photocatalytic H_2 Evolution over TiO_2 Nanoparticles. The Synergistic Effect of Anatase and Rutile. *J. Phys. Chem. C* **2010,** *114* (6), 2821-2829.

59. Ma, T.; Akiyama, M.; Abe, E.; Imai, I., High-Efficiency Dye-Sensitized Solar Cell Based on a Nitrogen-Doped Nanostructured Titania Electrode. *Nano Lett* **2005,** *5* (12), 2543-2547.

60. Lindgren, T.; Mwabora, J. M.; Avendaño, E.; Jonsson, J.; Hoel, A.; Granqvist, C.-G.; Lindquist, S.-E., Photoelectrochemical and Optical Properties of Nitrogen Doped Titanium Dioxide Films Prepared by Reactive DC Magnetron Sputtering. *J. Phys. Chem. B* **2003,** *107* (24), 5709-5716.

61. Koo, H. S.; Wang, D. T.; Yu, Y. K.; Ho, S. H.; Jhang, J. Y.; Chen, M.; Tai, M. F., Effect of Cu_2O Doping in TiO_2 Films on Device Performance of Dye-Sensitized Solar Cells. *Jpn J Appl Phys* **2012,** *51* (10).

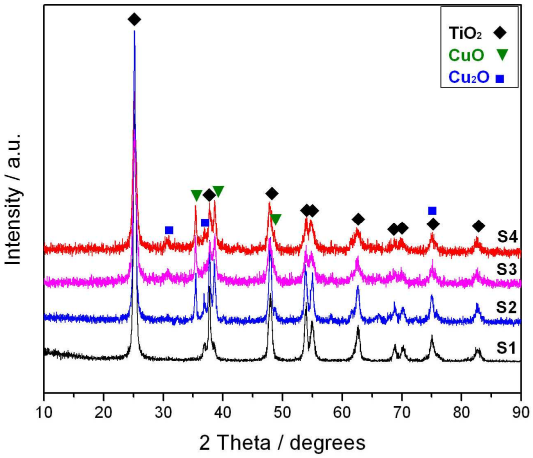

Figure 1 XRD patterns of TiO_2 and TiO_2/Cu_xO hybrids prepared under different concentrations of copper acetate monohydrate: (a) S1, (b) S2, (c) S3 and (d) S4.

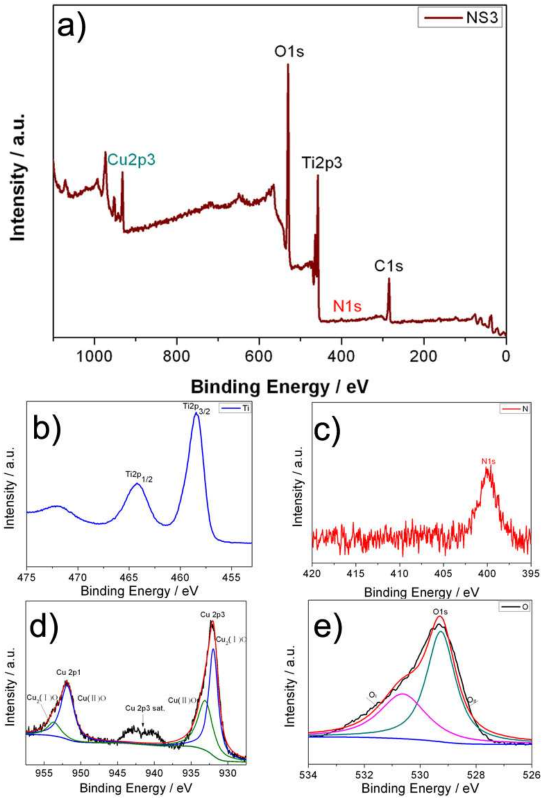

Figure 2 XPS spectrum of the N-doped TiO_2/Cu_xO sample: (a) survey spectrum, (b) Ti 2p spectrum, (c) Cu 2p spectrum and (d) O 1s spectrum.

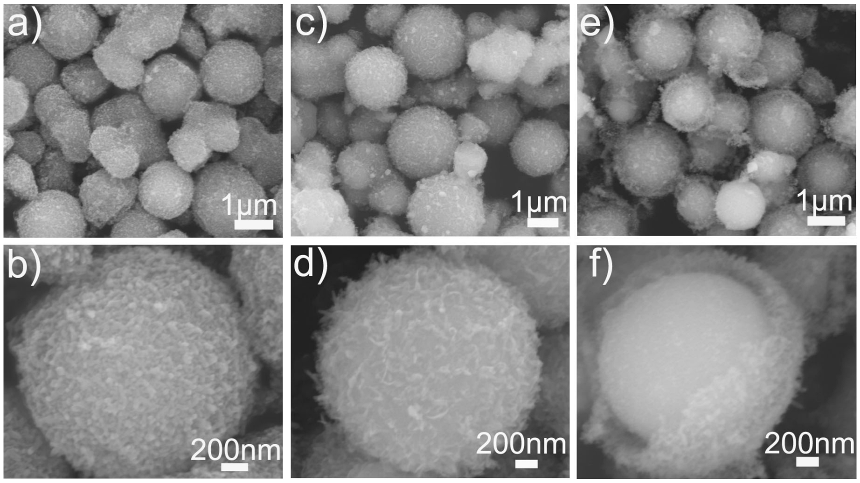

Figure 3 FE-SEM images of TiO_2/Cu_xO mesoporous beads prepared using different concentrations of copper acetate monohydrate: (a) (b) S2, (c) (d) S3 and (e) (f) S4.

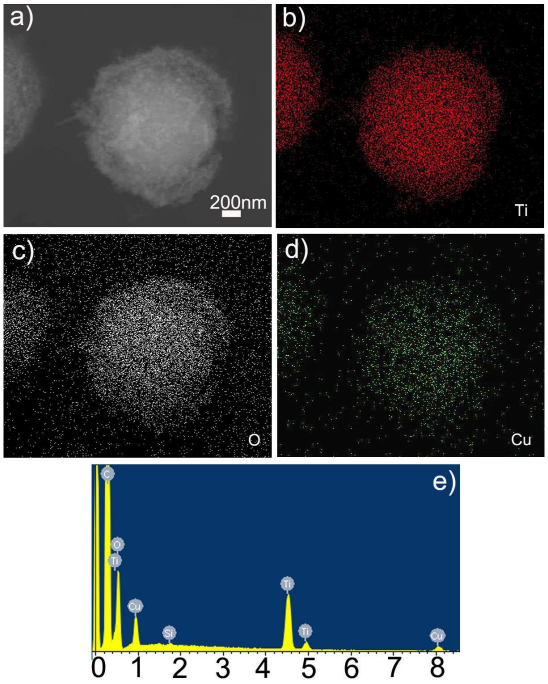

Figure 4 (a) (b) (c) (d) SEM image and Ti, O, Cu EDS mapping from TiO_2/Cu_xO core/shell hybrids (S4). (e) A typical EDS spectrum.

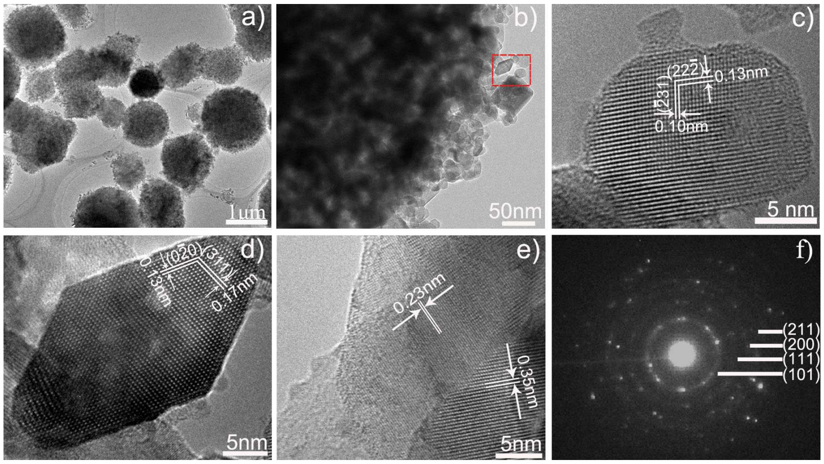

Figure 5 (a) A TEM image of TiO_2/Cu_xO hybrid (S3) prepared under 0.05 M copper acetate monohydrate. (b) A high-magnification TEM image taken from the edge of TiO_2/Cu_xO nanostructures. (c) A HRTEM lattice image of anatase TiO_2. The marked d-spacing of 0.13 nm and 0.10 nm correspond well to that of (22-2) and (-231) planes. (d) A HRTEM lattice image of Cu_2O nanoparticle. The marked d-spacing of 0.17 nm and 0.13 nm correspond well to that of (311) and (0-20) planes. (e) A HRTEM lattice image shows the TiO_2/Cu_xO nanostructure, the marked d-spacing of 0.35 nm and 0.23 nm is in agreement with that of (101) plane of TiO_2 and (111) plane of CuO. (f) Electron diffraction pattern from the TiO_2/Cu_xO nanostructures, the diffraction rings correspond to the (101), (200) and (211) planes of anatase TiO_2, (111) plane of CuO.

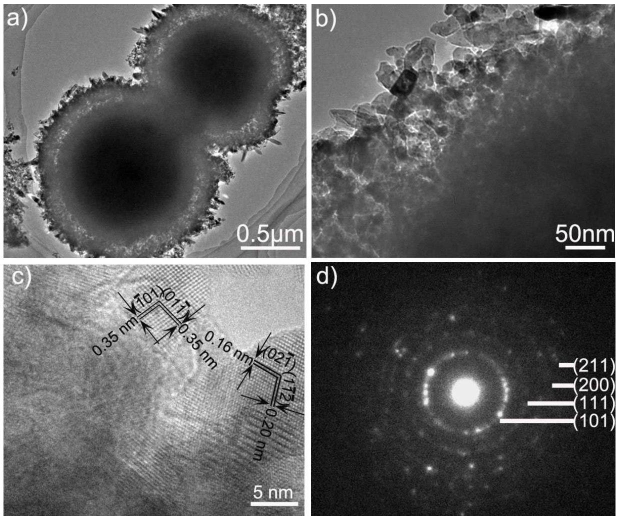

Figure 6 (a) A TEM image of TiO_2/Cu_xO core/shell hybrids prepared under 0.1 M copper acetate monohydrate. (S4) (b) A magnification TEM image taken from the shell's edge of TiO_2/Cu_xO core/shell nanostructures. (c) A HRTEM lattice image of anatase TiO_2 nanocrystal and Cu_xO nanoparticle. The marked d-spacing of 0.35 nm and 0.35 nm correspond well to (-101) and (01-1) planes of anatase TiO_2. The marked d-spacing of 0.20 nm and 0.16 nm correspond well to of (1-1-2) and (02-1) planes of monoclinic CuO. (d) Electron diffraction pattern from TiO_2/Cu_xO core/shell hybrids, the diffraction rings correspond to the (101), (200) and (211) planes of anatase TiO_2, (111) plane of CuO.

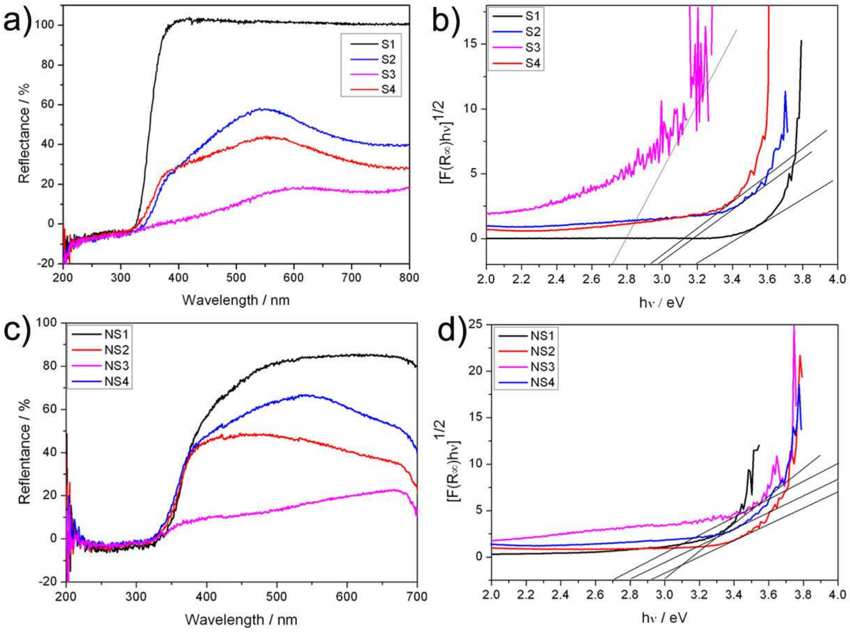

Figure 7(a) The UV-vis diffuse reflectance spectra (DRS) of the TiO_2 and TiO_2/Cu_xO hybrid samples. (b) The plots of transformed Kubelka-Munk function versus the energy of light. (c) The UV-vis diffuse reflectance spectra (DRS) of the N doped TiO_2 and N-doped TiO_2/Cu_xO samples. (d) The plots of transformed Kubelka-Munk function versus the energy of light.

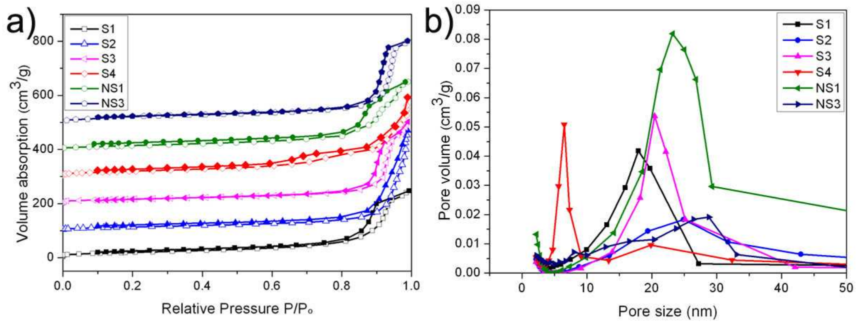

Figure 8 (a) N_2 adsorption-desorption curves and (b) pore size distribution plot for TiO_2, TiO_2/Cu_xO and N-doped TiO_2/Cu_xO samples (open symbols: adsorption; closed symbols: desorption).

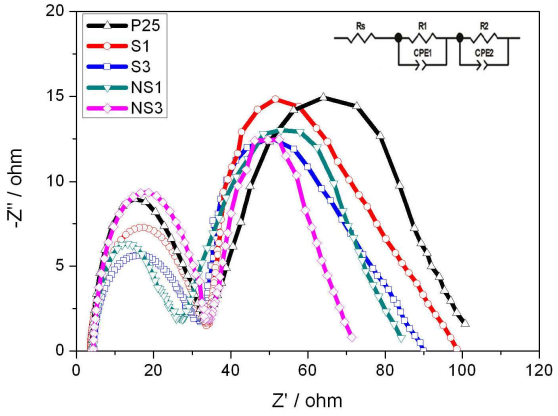

Figure 9 Nyquist impedance plots of (a) P25, (b) S1, (c) S3, (d) NS1 and (e) NS3 under one-sun irradiation. The frequency range was 10 mHz to 100 KHz; the magnitude of the alternating potential was 20 mV. The EIS spectra were fitted by ZSimpWin software using an equivalent circuit.

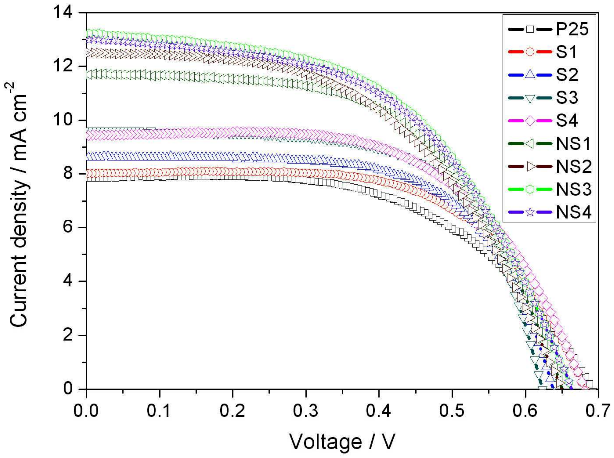

Figure 10 J-V curves of solar cells based on (a) P25, (b) S1, (c) S2, (d) S3, (e) S4, (f) NS1, (g) NS2, (h) NS3, and (i) NS4.

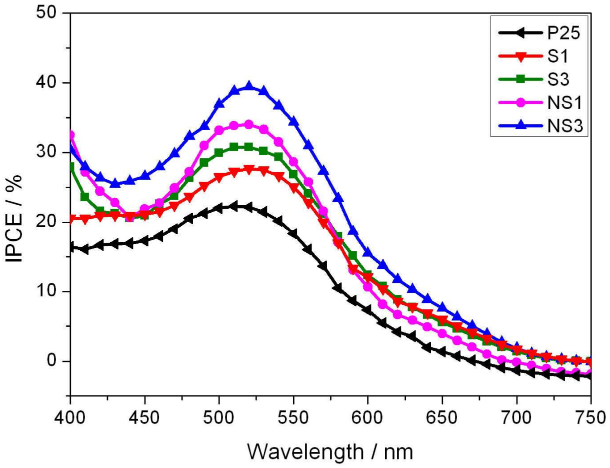

Figure 11 IPCE spectra of solar cells based on samples of (a) P25, (b) S1, (c) S3, (d) NS1 and (e) NS3.

Supporting Information

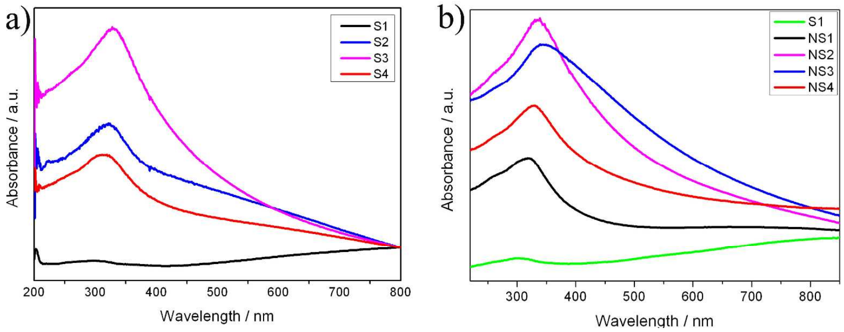

Figure S1 (a) UV–vis absorption spectra of TiO_2 (S1) and Cu_xO/TiO_2 samples. (b) UV–vis absorption spectra of TiO_2 (S1) and the nitrogen doped Cu_xO/TiO_2 samples.

The absorption spectra are employed to characterize the optical absorption performance of mesoporous TiO_2 and TiO_2/Cu_xO hybrids. Fig. S1a shows the UV–vis absorption spectra of mesoporous TiO_2 sample (S1), mesoporous TiO_2/Cu_xO hybrid samples of S2, S3, and S4, prepared under different concentrations of copper acetate monohydrate, respectively. The absorption spectra of the pure mesoporous TiO_2 sample (S1) shows weak absorption onset around 375 nm, which corresponds to the inherent band gap energy of pure TiO_2 (3.2 eV). As shown in Fig. S1a, the coupling of Cu_xO with the mesoporous induces a red-shift for the optical absorption edge from ultraviolet to visible region. Furthermore, the absorption peak and intensity of the mesoporous TiO_2/Cu_xO core/shell hybrids is affected by the contents of copper acetate monohydrate. It can be seen that the absorbance peak of mesoporous TiO_2/Cu_xO hybrid obtained under 0.05M copper acetate monohydrate is stronger, and displays an obvious red-shift of the absorption edge. It is suggested that the sample S3 shows the mostly enhanced ability to absorb visible-light, making it for promising application in photovoltaic devices.

In order to further improve the photoelectron conversion efficiency (η) of solar cells, we synthesize mesoporous N-doped TiO_2/Cu_xO core/shell hybrids. Fig. S1b shows the UV–vis absorption spectra of TiO_2 (S1), N-doped TiO_2 (NS1) and N-doped TiO_2/Cu_xO core/shell hybrids prepared under different concentrations of copper acetate monohydrate: NS2, NS3 and NS4 samples. The absorption edge for pure TiO_2 is observed at 385 nm (～3.2 eV), while the absorption edge for the N-doped TiO_2 sample (NS1) is at around 415 nm (～3.0 eV). Compared with un-doped TiO_2/Cu_xO core/shell hybrids (S2, S3, S4 samples), the N-doped TiO_2/Cu_xO core/shell hybrids (NS2, NS3 and NS4 samples), slightly red-shift takes place towards the visible spectral range. It could be ascribed to the combined effect of the doping-induced mid-gap electronic states and the lattice disorder effects due to the nitrogen doping. In the N–TiO_2 system the visible-light response arises due to occupied localized N2p states above the valence band. The doping also creates localized states below the conduction band edge. It is noted that prepared with the concentration of copper acetate monohydrate increasing, the N-doped TiO_2/Cu_xO hybrids display the same red-shift trend compared with Non N-doped TiO_2/Cu_xO hybrids. The absorption peak of the N-doped TiO_2/Cu_xO hybrids show a more obvious red-shift trend compared with that of the TiO_2/Cu_xO sample.

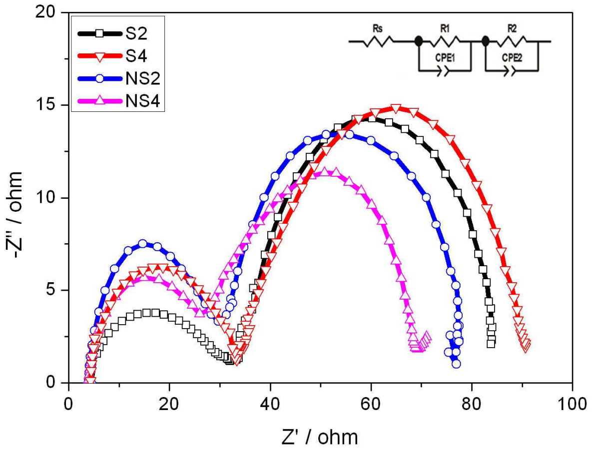

Figure S2 Nyquist impedance plots of (a) S2, (b) S4, (c) NS2, and (d) NS4 under one-sun irradiation. The frequency range was 10 mHz to 100 KHz; the magnitude of the alternating potential was 20 mV. The EIS spectra were fitted by ZSimpWin software using an equivalent circuit.

Table S1 Series resistances of the typical samples based DSSCs

Samples	R_S (Ω)	R_1(Ω)	R_2(Ω)
P25	4.0	28.7	67.7
S1	3.7	30.1	67.9
S2	4.2	28.8	57.3
S3	4.7	24.2	56.7
S4	4.3	29.1	57.5
NS1	4.3	29.9	56.8
NS2	4.0	26.4	45.5
NS3	4.2	29.1	36.9
NS4	3.9	22.1	43.4

To better understand the interfacial reactions of photoexcited electrons and the effect of film structure on the photovoltaic performance of DSSCs, the electrochemical impedance spectroscopy (EIS) measurements were performed to reveal the electron transport during the photovoltaic process of DSSCs.[1, 2] Fig. S2 shows the Nyquist plots of DSSCs based on S2, S4, NS2, and NS4 film electrodes. The equivalent circuit is shown as the inset in Fig. S2 using non-linear-least-square (NLLS) fit analysis software (Zview software) and all the fitting data are given in Table S1.

Rs can be recognized and fitted according to an equivalent circuit model as the sheet resistance of the FTO glass substrate and the contact resistance at FTO/TiO_2 (N-doped Cu_xO/TiO_2) interface.[3] The Rs values of DSSCs based on all the electrodes calculated according to the equivalent circuit were about 4 Ω, respectively. It is clear that the Rs of all the electrodes are very small, implying good electronic contact between TiO_2 (N-doped Cu_xO/TiO_2) materials and FTO. The small semicircle in the high frequency region is related to the charge transfer resistance (R_1) and interfacial capacitance (CPE_1) at interfaces between the electrolyte and Pt electrode.[4] The electron transport resistance (R_2) at intermediate frequency and interfacial capacitance (CPE_2) give information on the impedance at the TiO_2 (N-doped Cu_xO/TiO_2)/electrolyte interface.[5]

In particular, the electron transport resistance (R_2) plays a vital role in the photovoltaic performance of DSSCs in that it is related to the number of electrons going back to the electrolyte at the TiO_2 (N-doped Cu_xO/TiO_2)/electrolyte interface.[5] The R_2 values of DSSCs based on P25-NS4 electrodes calculated according to the equivalent circuit were showed in Table S1. The R_2 values of DSSCs based on P25, S1, and NS1 electrodes calculated according to the equivalent circuit were 67.7, 67.9, and 56.8 Ω, respectively. The R_2 values of P25 and un-doped TiO_2 (S1) samples are much of a size, while the R_2 of the N-doped TiO_2 (NS1) sample is a little less than that of P25 and S1 samples, which indicates that the nitrogen doped has a positive effect on the performance improvement. Compared with un-doped TiO_2/Cu_xO core/shell hybrids (S2, S3, and S4 samples); it is clearly that the R_2 of the N-doped TiO_2/Cu_xO core/shell hybrids (NS2, NS3, and NS4) samples is smaller than that of P25 and TiO_2/Cu_xO core/shell hybrids samples. It indicates that electrons are easier to move in the N-doped TiO_2/Cu_xO core/shell hybrid samples and thus contributes to improved charge transport ability. In particular, the R_2 of NS3 electrode is the smallest (36.9 Ω), corresponding to the highest performance of solar cells.

References

1. Longo, C.; Nogueira, A. F.; De Paoli, M. A.; Cachet, H., Solid-State and Flexible Dye-Sensitized TiO_2 Solar Cells: a Study by Electrochemical Impedance Spectroscopy. *J. Phys. Chem. B* **2002,** *106* (23), 5925-5930.
2. Wang, Q.; Ito, S.; Grätzel, M.; Fabregat-Santiago, F.; Mora-Seró, I.; Bisquert, J.; Bessho, T.; Imai, H., Characteristics of High Efficiency Dye-Sensitized Solar Cells†. *J. Phys. Chem. B* **2006,** *110* (50), 25210-25221.
3. Yu, J.; Li, Q.; Shu, Z., Dye-sensitized solar cells based on double-layered TiO_2 composite films and enhanced photovoltaic performance. *Electrochim Acta* **2011,** *56* (18), 6293-6298.
4. Yoshida, Y.; Tokashiki, S.; Kubota, K.; Shiratuchi, R.; Yamaguchi, Y.; Kono, M.; Hayase, S., Increase in photovoltaic performances of dye-sensitized solar cells-Modification of interface between TiO_2 nano-porous layers and F-doped SnO_2 layers. *Sol Energ Mat Sol C* **2008,** *92* (6), 646-650.
5. Hoshikawa, T.; Yamada, M.; Kikuchi, R.; Eguchi, K., Impedance Analysis of Internal Resistance Affecting the Photoelectrochemical Performance of Dye-Sensitized Solar Cells. *J Electrochem Soc* **2005,** *152* (2), E68.